LEARNING MULTI-GRANULARITY VISUAL-TEXTUAL ALIGNMENT FOR ZERO-SHOT ANOMALY DETECTION

Anonymous authors
Paper under double-blind review

ABSTRACT

Utilizing a detection model trained on an auxiliary dataset to detect anomalies has shown strong potential for zero-shot anomaly detection (ZSAD). However, prior approaches typically rely on text prompts with single-level visual-textual representations, hindering the detection of anomalies that vary in shape and appearance. To address this limitation, we propose a generalized ZSAD framework that empowers visual-textual representations from coarse-grained alignment to multi-granularity alignment. On the textual side, we expand the traditional single-level alignment into a multi-level paradigm. Different from previous work that ensembles multiple prompts with limited perception, we novelly assign prompts with multiple receptive fields to facilitate the learning of structured visual semantics at different levels of granularity. This constitutes our MPA approach. Building upon MPA, we further enhance visual granularity by employing different experts for fine-grained modeling of visual patch tokens. To this end, we propose a Mixture-of-Experts adaptation mechanism that dynamically routes patch tokens to multiple experts from a shared expert pool. This allows the selected experts, each with specialized knowledge, to collaboratively represent visual tokens at multiple granularities. These components constitute our MPAMA framework. We evaluate both MPA and MPAMA on datasets across industrial and medical domains. Extensive experiments demonstrate that our method outperforms state-of-the-art approaches.

1 INTRODUCTION

Anomaly detection plays a vital role in various applications, including industrial inspection (Bergmann et al., 2019; Huang et al., 2022; Chen et al., 2022; Bergmann et al., 2020; You et al., 2022; Liznerski et al., 2021; Gu et al., 2024b; Gao, 2024) and medical diagnosis (Pang et al., 2021; Qin et al., 2023; Liu et al., 2023). With the advent of the pre-trained model era, anomaly detection has evolved from small models trained from scratch (Xie et al., 2023; Ding et al., 2022) to generalized architectures pre-trained on large-scale datasets (Radford et al., 2021; Zhou et al., 2022b; Jeong et al., 2023; Zhou et al., 2024a;b). The scope of detection has also broadened from category-specific designs to models capable of handling diverse objects.

Recent ZSAD approaches (Zhou et al., 2024a; Cao et al., 2024; ZHU et al., 2025; Chen et al., 2022; Jeong et al., 2023) leverage the strong generalization capabilities of large pretrained vision-language models such as CLIP (Radford et al., 2021), and have demonstrated strong potential in detecting anomalies on previously unseen objects. These methods typically employ single-level textual and visual representations to align with semantic-rich local visual features. However, they face two key limitations in Figure 1(a): (1) **Single-level alignment:** Anomalies can vary significantly in spatial scale, ranging from a tiny hole on a screw to a large crack in a hazelnut. Relying on a single-scale alignment limits the model to capturing such diverse anomaly patterns; (2) **Lack of visual granularity:** A single visual expert shared across all patch tokens restricts the model's capacity to represent anomaly patterns at varying levels of granularity.

To address these, we propose a novel multiple-granularity framework designed to empower the limited textual and visual representation for accurate anomaly semantics learning. As illustrated in Figure 1(b), we present two innovations to advance the cross-modal alignment of CLIP from a granularity-aware perspective. On the text side, unlike previous work that relies on single or ensemble text prompts with limited perception to align visual embeddings, we propose multi-perception

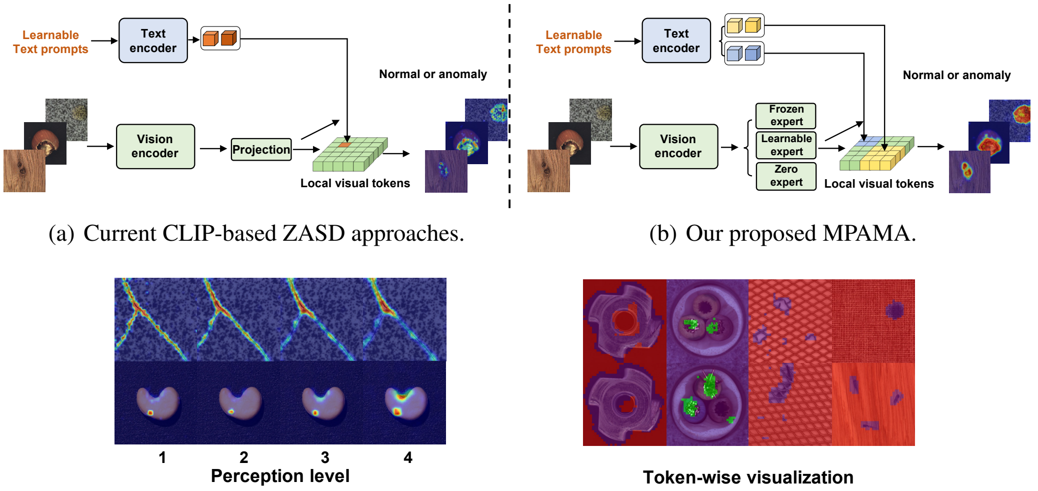

(a) Current CLIP-based ZASD approaches.

(b) Our proposed MPAMA.

(c) Segmentation visualization.

(d) Token-wise expert assignment.

Figure 1: Motivation of MPAMA. **(a)**: Current CLIP-based ZSAD methods typically rely on single-perception and coupled text prompts to align limited visual representations. **(b)**: In contrast, our approach introduces powerful textual and visual representations to mitigate the conflict between coarse-grained classification and fine-grained segmentation. **(c)**: Text prompts with small receptive fields (e.g., receptive fields of 1 and 2) are effective at detecting small-scale anomalies but are more susceptible to noise. In contrast, prompts with large perceptual fields are more robust to noise but tend to miss small anomalies. **(d)**: Experts capture distinct visual patterns. For example, the red expert primarily focuses on background and texture, the purple expert captures object regions and anomalies with large semantics variation, and the green expert tends to respond to deformations.

alignment that enriches text prompts with distinct receptive fields. This allows each prompt to be aware of structured and spatial anomalies at specialized scales. By ensembling these prompts, the model becomes capable of capturing anomalies across a wide range of scales in Figure 1(c).

Building on this, we aim to enhance visual granularity by replacing the traditional single shared expert with multiple specialized experts. To this end, we introduce Mixture-of-Experts adaptation (MA), which dynamically routes visual tokens to appropriate experts (Lepikhin et al., 2021). The selected experts, each with diverse specialized knowledge, jointly represent visual patch tokens at multiple levels of granularity, as illustrated in Figure 1(d). These components constitute the complete MPAMA framework. The main contributions of this paper are summarized as follows:

- We reveal that single-level alignment in existing ZSAD approaches hinders the model's ability to learn comprehensive anomaly semantics. To address this limitation, we propose MPA and MPAMA, which enhance visual-textual representation by extending coarse-grained alignment to multi-granularity alignment, enabling holistic anomaly learning.
- We expand traditional single-level alignment into a multi-level paradigm. Learnable text prompts are enriched with distinct perceptual fields to capture anomaly semantics at different receptive fields. These prompts are jointly optimized to incorporate anomaly semantics across multiple granularities.
- A single shared visual expert is insufficient to represent all visual patch tokens. To overcome this, we propose MA, which dynamically routes each patch token to multiple experts, each possessing specialized knowledge. The selected experts collaboratively represent the patch token from different granularities.
- Extensive experiments on datasets spanning a wide range of object categories have been conducted to demonstrate the effectiveness of MPA and MPAMA. The results consistently show superior performance in both anomaly detection and segmentation tasks.

2 PRELIMINARY

Problem Formulation Given an auxiliary dataset comprising normal and abnormal images $x \in \mathcal{R}^{3\times H_{\text{image}}\times W_{\text{image}}}$ with their corresponding labels, i.e., $y \in \mathcal{R},\ S \in \mathcal{R}^{H_{\text{image}}\times W_{\text{image}}}$, our objective is to train a zero-shot anomaly detection model capable of generalizing to previously unseen samples

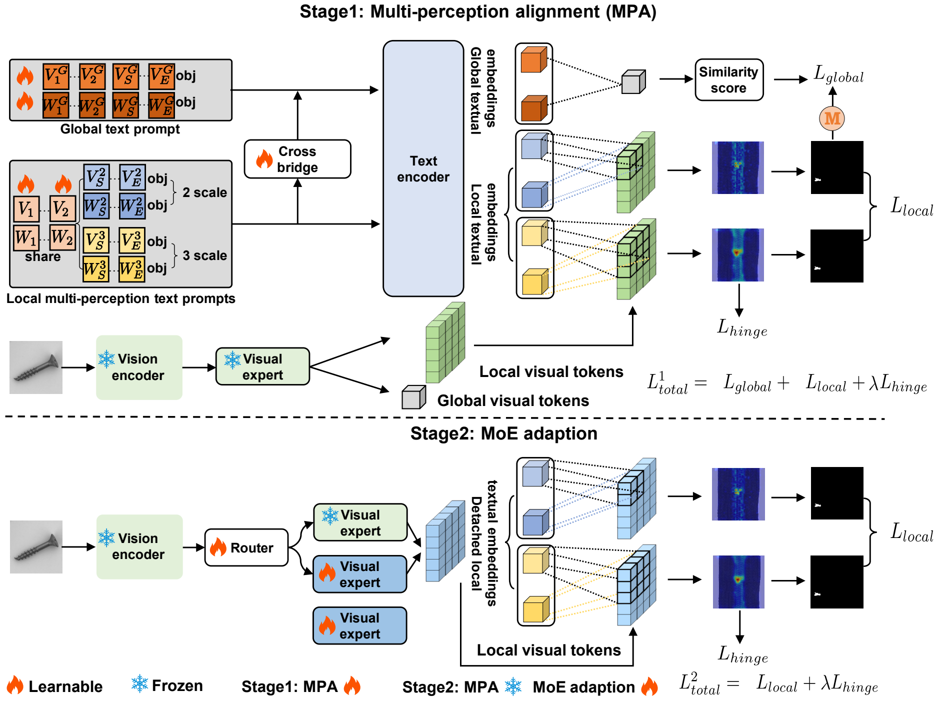

Figure 2: Overview of MPAMA. Our model consists of two stages. In Stage 1, we propose MPA to adapt the textual space of CLIP while keeping the visual space frozen. We introduce multi-perception text prompts to capture anomaly patterns at multiple spatial scales, enabling comprehensive semantic modeling. To further enhance representation, local and global text prompts are disentangled to mitigate the semantic coupling between fine-grained segmentation and coarse-grained classification. In Stage 2, we freeze the textual space and adapt the visual space by introducing specialized visual experts. These experts enhance the model's ability to represent complex and diverse anomaly patterns.

across different categories and domains. Note that 0 indicates normality and 1 indicates abnormality. The detection model is expected to perform anomaly classification $\mathcal{A}_c(x) : \mathcal{R}^{3\times H_{\text{image}}\times W_{\text{image}}} \mapsto \mathcal{R}$ and anomaly segmentation, defined as $\mathcal{A}_s(x) : \mathcal{R}^{3\times H_{\text{image}}\times W_{\text{image}}} \mapsto \mathcal{R}^{H_{\text{image}}\times W_{\text{image}}}$.

A Brief Review of CLIP for Classification and Segmentation Given a learnable text prompt template G for class c, the text encoder $T(\cdot)$ generates the corresponding textual embedding, denoted as $g_c = T(G_c) \in \mathcal{R}^D$. In the context of anomaly detection, the task involves classifying two classes: *normal* and *abnormal*. Accordingly, we define the text embeddings as $g_n = T(G_n)$ and $g_a = T(G_a)$, where G_n and G_a are the learnable prompts corresponding to the normal and abnormal classes, respectively. The vision encoder $F(\cdot)$ processes an input image x to extract its visual representations $[\bar{f}, \bar{v}] = F(x)$. A projection layer $h(\cdot)$ projects them into class token $f = h(\bar{f})$ and patch tokens $v = h(\bar{v})$, where $f \in \mathcal{R}^D$ and $v \in \mathcal{R}^{H\times W\times D}$. These tokens are ℓ_2-normalized by default. CLIP enables zero-shot anomaly detection by computing the similarity between textual and visual tokens. The image-level and patch-level abnormality possibilities are calculated as

$$P(g_a, f) = \frac{\exp(\langle g_a, f\rangle/\tau)}{\sum_{c\in\{n,a\}} \exp(\langle g_c, f\rangle/\tau)}, \qquad P(g_a, v^i) = \frac{\exp(\langle g_a, v^{(i,j)}\rangle/\tau)}{\sum_{c\in\{n,a\}} \exp(\langle g_c, v^i\rangle/\tau)},$$

where τ is a temperature hyperparameter and $\langle\cdot,\cdot\rangle$ denotes cosine similarity. We derive the segmentation of position i as $S_a(i) = P(g_a, v_i)$, resulting in segmentation maps $S_n, S_a \in \mathcal{R}^{H\times W}$.

3 Methods

Overview This paper aims to enhance CLIP's visual-textual representations by extending coarse-grained alignment to multi-granularity alignment, enabling accurate zero-shot anomaly detection across diverse categories. As illustrated in Figure 2, the proposed framework consists of two main components: MPA and MA, which together adapt CLIP in both the textual and visual embedding spaces. In the first stage (MPA), we adapt the textual space through MPA. In the second stage (MPAMA), we freeze the text encoder and adapt the visual space via MA.

3.1 Multi-perception alignment

Unseen anomalies typically appear at various scales and shapes. Prior works (Zhou et al., 2024a; Qu et al., 2025) that rely on single-level alignment often struggle to capture such diverse patterns. To address this limitation, we propose MPA, which captures anomalies of varying sizes and structures simultaneously. This enhances the model's generalization ability to detect a broader range of anomalies. Specifically, we define a set of learnable multi-scale text prompt templates $L = \{L^p\}_{p \in \mathcal{P}}$, where each $L^p = \{L_n^p, L_a^p\}$ contains the normality and abnormality prompts corresponding to perception level p, and $\mathcal{P}$ denotes the set of selected perception levels.

$$L_n^p = [V_1^p][V_2^p]\cdots[V_E^p][object] \qquad L_a^p = [W_1^p][W_2^p]\cdots[W_E^p][damaged][object].$$

where $[V_i^p]$ and $[W_i^p]$ ($V_i^p, W_i^p \in \mathcal{R}^D$) are learnable word embeddings in normality and abnormality text prompt templates of perception p, respectively. Each prompt is mapped through the text encoder to produce a scale-aware text embedding $\ell_c^p = T(L_c^p)$. To associate each text embedding with spatial visual context, we compute its similarity with an aggregated visual token at each spatial location i using a generalized local aggregation operator. This provides each position with a broader receptive field, allowing the model to capture structural patterns, such as anomaly boundaries and large contiguous regions. In contrast, visual tokens with limited perceptual fields are prone to misdetecting large-scale anomalies due to insufficient contextual awareness. Formally, we define a generalized local aggregation operator $\mathcal{A}_p(v_i)$ over a $p \times p$ neighborhood $\mathcal{N}_p(i)$ centered at position i. The aggregated token v_i^p is computed as:

$$v_i^p = \mathcal{AGG}_p(v_i) = \text{AGG}\left(\{v_j \mid j \in \mathcal{N}_p(i)\}\right),$$

where $\mathcal{AGG}_p(\cdot)$ denotes a generic aggregation function used to summarize the local patch tokens. Common choices include average pooling, max pooling, or learnable alternatives such as attention mechanisms or small MLPs. In this work, we focus on average pooling and leave max pooling learnable aggregation strategies for future exploration. The segmentation at location i under perception level p is rewritten as:

$$S_a^p(i) = P(\ell_a, v_i^p) = \frac{\exp\left(\langle \ell_a^p, v_i^p \rangle / \tau\right)}{\sum_{c \in \{n,a\}} \exp\left(\langle \ell_c^p, v_i^p \rangle / \tau\right)}. \tag{1}$$

In doing so, L^p is used to learn anomalies at scale p. We then ensemble text prompts with different perceptions to capture anomalies of varying sizes. To facilitate anomaly learning in different scales, we share the prefix portion of the learnable embeddings across text prompt templates with different perceptions. The resulting multi-perception prompt template is defined as:

$$L_n^p = [V_1]\cdots[V_S][V_{S+1}^p]\cdots[V_E^p][object], L_a^p = [W_1]\cdots[W_S][W_{S+1}^p]\cdots[W_E^p][damaged][object].$$

The $[V_i]$ and $[W_i]$ ($i \in 1, \ldots, S$) are shared learnable word embeddings in normality and abnormality text prompt templates across the perception levels.

We aim to simultaneously model global and local anomaly semantics for classification and segmentation. Existing works typically employ shared text prompts to learn global and local anomaly semantics. However, this coupling introduces an alignment compromise between the two objectives.

Anomaly classification requires prompt templates to identify an image as anomalous if it contains any abnormal region, even when most of the pixels are normal. In contrast, anomaly segmentation demands fine-grained prompts capable of distinguishing each pixel as normal or abnormal. From the perspective of classification, focusing too heavily on pixel-level semantics can impair the model's ability to capture high-level anomaly concepts, since anomalous images often contain large regions of normal content. Conversely, emphasizing global semantics can weaken the model's sensitivity to localized specific anomaly pixels, thereby impairing precise pixel-wise discrimination. This conflict indicates that using coupled prompt templates for both global and local tasks imposes a compromise, potentially degrading performance on both fronts. To resolve this, we propose to disentangle the prompts into two distinct branches: global prompts and local prompts, each optimized for its respective objective. Formally, we define the global text prompts as follows:

$$G_n = [V_1^G]\cdots[V_E^G][object], \;\; G_a = [W_1^G]\cdots[W_E^G][damaged][object]. \tag{2}$$

To further improve global semantic modeling, we introduce a cross-level bridging mechanism that transfers salient features of local prompts to the global prompt. This allows the global prompt to maintain a holistic view while benefiting from fine-grained local features.

Let $\bar{G}_a \in \mathcal{R}^{E\times D}$ and $\{\bar{L}_a^p\}_{p\in\mathcal{P}}$ be the learnable parts of global and local prompt embeddings for the abnormal class. We compute the element-wise maximum of $\{\bar{L}_a^p\}_{p\in\mathcal{P}}$ along the perception levels: $\bar{L}_a^{\max} = \max_p\{\bar{L}_a^p\}_{p\in\mathcal{P}}$. $\bar{L}_a^{\max} \in \mathcal{R}^{E\times D}$ is salient feature from local prompts. Then we integrate the salient feature with global prompt embeddings to the final $\tilde{G}_a$ by concatenating $\bar{G}_a$ with $\bar{L}_a^{\max}$ along the channel, followed by an MLP. The mathematical formulation is given by:

$$\tilde{G}_a = \text{MLP}\left(\text{Concat}(\bar{G}_a,\ \max_p\{\bar{L}_a^p\}_{p\in\mathcal{P}})\right),\ \ \tilde{G}_n = \text{MLP}\left(\text{Concat}(\bar{G}_n,\ \max_p\{\bar{L}_n^p\}_{p\in\mathcal{P}})\right).$$

These lead to MPA, which adapts the textual space of CLIP for fine-grained anomaly modeling.

3.2 Multi-granularity visual representation via MoE Adaptation

Through MPA, the text space is adapted to handle anomalies with multiple levels of granularity. Here, we freeze the textual space and instead adapt the visual space to achieve multi-granular visual modeling. We treat the projection of the original visual encoder as the expert. Previous works replace the expert to learn a new expert from scratch. However, such an expert is limited in capturing the complex distribution and is easily overfitting to the auxiliary dataset, thus decreasing the generalization capacity. We propose MA to dynamically route visual tokens to multiple specialized experts, enabling joint representation of each patch token at multiple granularities. Unlike standard MoE approaches that rely on homogeneous experts, we define three types of experts: **learnable experts** h^l, **frozen experts** h^f, and **zero experts** $h^z(v_i) = 0$. For the frozen expert, the intuition is that certain pretrained experts already perform well on specific visual patterns and thus do not require further tuning. In contrast, learnable experts are essential for handling tokens with novel or unseen patterns, enabling the model to specialize in anomaly semantics through training. Lastly, some tokens could be sufficiently represented by a single expert. The zero expert provides a unified modeling mechanism by zeroing out the input.

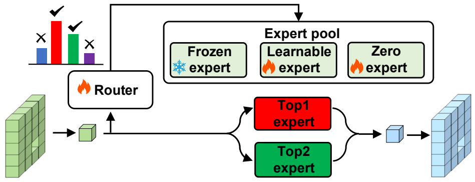

Figure 3: Overview of MOE adaptation.

Specifically, we first define the expert pool $\mathcal{H} = \{h_0^f, h_1^l, h_2^l, h_3^l, \cdots, h_N^z\}$. Considering the original expert contains generic prior knowledge, we use its weight as the initialization of all experts. Then, we use the trainable weight matrix $w \in \mathcal{R}^{D\times N}$ as the learnable router $\text{Ro}(\bar{v}_i) = w\bar{v}_i$, which decides to route tokens to specialized experts. v is the final weighted sum of outputs from K activated experts:

$$v_i = \sum_{i=0}^{N} e_i h_i(\bar{v}_i),\ \ e_i = \begin{cases} \text{Softmax}(\text{Ro}(\bar{v}_i)), & \text{if } \text{Ro}(\bar{v}_i) \in \text{Top-K}\left(\{\text{Ro}(\bar{v}_i) \mid 0 \le i \le N\}\right), \\ 0, & \text{otherwise.} \end{cases}$$

To sufficiently optimize on the router, we aggregate over $\bar{v}_i$ instead of v_i, i.e, $\bar{v}_i^p = \mathcal{AGG}_p(\bar{v}_i)$, and then feed them into the router, i.e., $\text{Ro}(\bar{v}_i^p) = w\mathcal{AGG}_p(\bar{v}_i), p \in \mathcal{P}$. The pre-aggregation increases the quantity and diversity of tokens input to the MoE compared to $\text{Ro}(\bar{v}_i)$ in the post-aggregation. The final output is rewritten as $v_i^p = \sum_{i=0}^{N} e_i h_i(\mathcal{AGG}_p(\bar{v}_i))$ different from $v_i^p = \mathcal{AGG}_p(\sum_{i=0}^{N} e_i h_i(\bar{v}_i))$ in the post-aggregation.

Multiple-perception Context Optimization Given the global text prompts $\tilde{G}_a$ and $\tilde{G}_n$, we could obtain the text embeddings $\tilde{g_a}$ and $\tilde{g_n}$ for abnormality and normality. We define L_{global} as a cross-entropy loss to align the image-level anomalies:

$$L_{global} = \text{CrossEntroy}([P(\tilde{g_n}, f], P(\tilde{g_a}, f)], y) \tag{3}$$

Given the local text prompts $\{L_a^p\}_{p\in\mathcal{P}}$ and $\{L_n^p\}_{p\in\mathcal{P}}$, our text prompts learn pixel-level multi-perception anomaly semantics by minimizing the following local loss:

$$L_{local} = \textstyle\sum_{p\in\mathcal{P}} \text{Focal}(\text{Up}([S_n^p, S_a^p]), S) + \text{Dice}(\text{Up}(S_n^p), I - S) + \text{Dice}(\text{Up}(S_a^p), S), \tag{4}$$

where $\text{Focal}(\cdot)$, $\text{Dice}(\cdot)$, and $\text{Up}(\cdot)$ denote the Focal loss (Lin et al., 2017), Dice loss (Li et al., 2019), and upsampling interpolation operation, respectively. To better separate normal and abnormal regions, we employ a hinge loss that encourages a larger margin between their respective anomaly scores:

$$L_{\text{hinge}} = \textstyle\sum_{p\in\mathcal{P}} \left(\frac{1}{|\mathcal{N}_0|} \sum_{i\in\mathcal{N}_0} \max\left(S_a^p(i) - \delta_n,\ 0\right) + \frac{1}{|\mathcal{N}_1|} \sum_{i\in\mathcal{N}_1} \max\left(\delta_a - S_a^p(i),\ 0\right) \right),$$

where $\mathcal{N}_0 = \{(i) \mid S(i) = 0\}$ and $\mathcal{N}_1 = \{(i) \mid S(i) = 1\}$ denote the sets of normal and anomalous pixels, respectively. $\delta_n \in \mathcal{R}$ and $\delta_a \in \mathcal{R}$ are the margin thresholds for normal and anomaly regions. This loss ensures that scores in normal regions remain below δ_n, while encouraging anomaly scores in anomalous regions to exceed δ_a.

MPAMA consists of two main components that adapt CLIP in both textual and visual spaces: MPA and MA. We adopt a two-stage training framework. Stage 1: Adapt the textual space via Multi-perception prompt learning, resulting in MPA. The total loss L_{total} jointly optimizes both local and global semantics with hinge loss regularization:

$$L^1_{total} = L_{global} + L_{local} + \lambda L_{hinge}. \tag{5}$$

Stage 2: The textual space is frozen, and the visual space is adapted using MA to align local semantics. This leads to the complete MPAMA. The corresponding loss is defined as:

$$L^2_{total} = L_{local} + \lambda L_{hinge}, \tag{6}$$

where λ is a weighting coefficient used to balance the three loss components.

Inference During Inference, we compute the final anomaly segmentation by averaging the segmentation maps across all perception levels: $\mathcal{A}_s(x) = \frac{1}{|\mathcal{P}|}\sum_{p \in P} S^p_a$. As for image-level anomaly detection, we integrate the global text similarity score and the maximum of the segmentation map: $\mathcal{A}_c(\cdot) = \frac{1}{2}P(\tilde{g_a}, f) + \frac{1}{2}\max(S_a)$.

4 Experiments

4.1 Experiment setup

Dataset Details & Baselines To comprehensively demonstrate the generalized zero-shot anomaly detection capability of MPAMA, we conducted extensive evaluations on publicly available datasets spanning a wide range of semantic categories across industrial and medical domains. For industrial inspection, we include MVTec AD (Bergmann et al., 2019), VisA (Zou et al., 2022), MPDD (Jezek et al., 2021), BTAD (Mishra et al., 2021), SDD (Tabernik et al., 2020), DAGM (Wieler & Hahn, 2007), and DTD-Synthetic (Aota et al., 2023). In the medical domain, we evaluate on datasets for skin cancer diagnosis (ISIC (Gutman et al., 2016)), colon polyp detection (CVC-ClinicDB (Bernal et al., 2015), CVC-ColonDB (Tajbakhsh et al., 2015), Kvasir (Jha et al., 2020), Endo (Hicks et al., 2021)), brain tumor detection (HeadCT (Salehi et al., 2021), BrainMRI (Salehi et al., 2021), and Br35H (Hamada., 2020)). Dataset and baseline details see Appendix A and B. † denotes results taken from original papers.

Evaluation Setting and Metrics We report AUROC and Average Precision (AP) to measure detection performance, and use AUROC and AUPRO to evaluate segmentation performance. All metrics are averaged over five runs. Following AnomalyCLIP, we use the MVTec AD dataset as the auxiliary training set for evaluating other datasets, and vice versa, training on VisA for MVTec AD.

Implementation Details We use the publicly available CLIP model (`ViT-L/14@336px`) as the backbone. We follow the data processing of AnomalyCLIP. All images are resized to 518 × 518. The length of the learnable embedding is set to $E = 12$, with a shared prefix length of $S = 2$. The perception set is defined as $\mathcal{P} = \{1, 2, 3, 4\}$. We use the top feature of the vision encoder as the visual representations, and use average pooling as the aggregation operator $\mathcal{AGG}$. The number of experts is set to 4 for training on VisA and 5 for MVTec AD, with 2 activated experts. We set the hinge loss thresholds to $\delta_a = \delta_n = 0.5$, and the weighting coefficients to $\lambda = 5$. We also provide the ablation study of λ in Appendix F. We use Adama optimizer with a learning rate of 1e-3 in stage 1 and 1e-6 in stage 2. The batch size is set to 8, and the training epoch is 30 in stage 1 and 10 in stage 2. All experiments are conducted using PyTorch 2.0.0 on a single NVIDIA RTX 3090 (24GB) GPU.

4.2 Main Results

Generalized ZSAD for Industrial Anomaly Detection We compare our models, MPA and MPAMA, with SOTA ZSAD baselines, including WinCLIP, VAND, CoOp, AdaCLIP, and AnomalyCLIP, across seven industrial datasets covering over 60 semantic categories. As shown in Table 1, our models consistently outperform baselines in both anomaly detection and segmentation tasks. For image-level detection, on the MVTec AD dataset, MPA achieves 94.1% AUROC and 96.9% AP, surpassing AnomalyCLIP's 91.5% AUROC and 96.2% AP. On the VisA dataset, MPA reaches

Table 1: ZSAD performance on industrial domain datasets. Best: Red; Second-best: Blue. † denotes results taken from original papers.

Task	Dataset	WinCLIP	VAND	AdaCLIP	AnomalyCLIP	FAPromt	MPA	MPAMA
		(CVPR'23)	(ARXIV'23)	(ECCV'24)	(ICLR'24)	(ICCV'25)	(Ours)	(Ours)
Image-level (AUROC, AP)	MVTec AD	(91.8, 96.5)†	(86.1, 93.5)†	(89.6, -)†	(91.5, 96.2)†	(90.8, 94.9)	(94.1, 96.9)	(94.5, 97.6)
	VisA	(78.1, 81.2)†	(78.0, 81.4)†	(83.8, -)†	(82.1, 85.4)†	(83.6, 85.6)	(85.0, 87.6)	(85.4, 88.0)
	MPDD	(63.6, 69.9)	(73.0, 80.2)	(76.8, -)†	(77.0, 82.0)†	(77.5, 82.2)	(79.4, 81.4)	(81.2, 82.1)
	BTAD	(68.2, 70.9)	(73.6, 68.6)	(88.6, -)†	(88.3, 87.3)†	(92.3, 93.0)	(89.0, 88.2)	(89.8, 88.9)
	SDD	(84.3, 77.4)	(79.8, 71.4)	(- , -)†	(84.7, 80.0)†	(81.8, 77.5)	(84.9, 80.8)	(85.2, 81.2)
	DAGM	(91.8, 79.5)	(94.4, 83.8)	(98.3, -)†	(97.5, 92.3)†	(96.9, 90.6)	(98.4, 92.9)	(98.5, 93.2)
	DTD-Synthetic	(93.2, 92.6)	(86.4, 95.0)	(95.5, -)†	(93.5, 97.0)†	(95.6, 97.4)	(96.2, 98.1)	(97.0, 98.8)
Pixel-level (AUROC, PRO)	MVTec AD	(85.1, 64.6)†	(87.6, 44.0)†	(90.3, -)†	(91.1, 81.4)†	(90.6, 81.6)	(92.5, 87.5)	(93.2, 88.3)
	VisA	(79.6, 56.8)†	(94.2, 86.8)†	(95.6, -)†	(95.5, 87.0)†	(95.6, 86.7)	(95.8, 87.9)	(96.1, 88.6)
	MPDD	(76.4, 48.9)	(94.1, 83.2)	(96.4, -)†	(96.5, 88.7)†	(95.7, 85.6)	(96.5, 88.3)	(96.8, 89.2)
	BTAD	(72.7, 27.3)	(60.8, 25.0)	(92.1, -)†	(94.2, 74.8)†	(94.8, 75.1)	(95.3, 78.5)	(96.0, 79.1)
	SDD	(68.8, 24.2)	(79.8, 65.1)	(- , -)†	(90.6, 67.8)†	(92.5, 70.0)	(92.7, 73.9)	(93.9, 74.2)
	DAGM	(87.6, 65.7)	(82.4, 66.2)	(91.0, -)†	(95.6, 91.0)†	(98.1, 94.9)	(96.6, 91.9)	(97.0, 92.7)
	DTD-Synthetic	(83.9, 57.8)	(95.3, 86.9)	(96.9, -)†	(97.9, 92.3)†	(98.0, 92.2)	(98.3, 92.9)	(98.5, 93.8)

85.0% AUROC and 87.6% AP, outperforming both 83.8% AUROC of AdaCLIP and 82.1% AUROC and 85.4% AP of AnomalyCLIP. We attribute this superiority to fine-grained anomaly semantics modeling at multiple scales and disentanglement learning of global and local anomaly semantics. Building on MPA, MPAMA further improves performance, reaching 94.5% AUROC and 97.6% AP on MVTec AD, and 85.4% AUROC and 88.0% AP on VisA. These gains stem from multiple specialized visual experts through MoE adaptation, which enhances the model's capacity to represent complex and diverse anomaly patterns. In terms of anomaly segmentation, our model achieves consistent superiority. On MVTec AD, MPA achieves 92.5% AUROC and 87.5% PRO, while MPAMA improves this to 93.2% AUROC and 88.3% PRO, outperforming the previous best by 91.1% AUROC and 81.4% PRO of AnomalyCLIP. Similar trends are observed on MPDD, BTAD, and so on. These illustrated that our models could learn the generalized anomaly semantics from multi-scale anomalies.

Table 2: Cross-domain ZSAD performance on medical analysis. Best: Red; Second-best: Blue.

Task	Dataset	WinCLIP	VAND	AdaCLIP	AnomalyCLIP	FAPromt	MPA	MPAMA
		(CVPR'23)	(ARXIV'23)	(ECCV'24)	(ICLR'24)	(ICCV'25)	(Ours)	(Ours)
Image-level (AUROC, AP)	HeadCT	(81.8, 80.2)	(89.1, 89.4)	(91.5, -)	(93.4, 91.6)	(93.9, 92.6)	(96.2, 96.0)	(96.4, 96.2)
	BrainMRI	(86.6, 91.5)	(89.3, 90.9)	(94.8, -)	(90.3, 92.2)	(94.8, 93.7)	(95.0, 95.8)	(95.6, 96.0)
	Br35H	(80.5, 82.2)	(93.1, 92.9)	(97.7, -)	(94.6, 94.7)	(96.6, 95.6)	(97.9, 97.9)	(98.1, 98.0)
Pixel-level (AUROC, PRO)	ISIC	(83.3, 55.1)	(89.4, 77.2)	(88.3, -)	(89.7, 78.4)	(90.7, 80.3)	(92.7, 85.2)	(93.5, 85.8)
	ColonDB	(70.3, 32.5)	(78.4, 64.6)	(79.1, -)	(81.9, 71.3)	(84.1, 73.2)	(83.9, 72.4)	(84.9, 72.6)
	ClinicDB	(51.2, 13.8)	(80.5, 60.7)	(84.4, -)	(82.9, 67.8)	(83.9, 69.3)	(84.6, 70.5)	(84.9, 70.3)
	Kvasir	(69.7, 24.5)	(75.0, 36.2)	(- , -)	(78.9, 45.6)	(80.4, 46.5)	(80.3, 45.7)	(81.9, 46.6)
	Endo	(68.2, 28.3)	(81.9, 54.9)	(- , -)	(84.1, 63.6)	(85.9, 65.0)	(87.1, 68.8)	(87.7, 69.5)

Cross-Domain Generalization from Industrial to Medical Domains The above results demonstrate that our models generalize well to industrial datasets. To further assess the generalization capability, we explore a more challenging cross-domain setting: train our model using the MVTec AD industrial dataset and directly test it on various medical tasks. As shown in Table 2, our models exhibit strong cross-domain generalization. Notably, for brain tumor detection, MPA achieves 96.2% AUROC on BrainMRI, while MPAMA further improves performance on HeadCT, surpassing AnomalyCLIP by increasing AUROC from 93.4% to 96.4% and AP from 91.6% to 96.2%. In the case of skin cancer detection, our models also demonstrate significant improvement. These results highlight the effectiveness and robustness of our proposed MPA and MPAMA frameworks, which generalize well beyond the source domain and adapt effectively to unseen domains.

4.3 Result Analysis

Multi-perception Prompt Learning vs. Single-perception Prompting Learning Here, we aim to investigate whether text prompts with different receptive fields can effectively capture anomalies at varying scales. We conduct a quantitative analysis to demonstrate our model's superior ability to detect anomalies across different scales. Specifically, we first count the number of anomaly pixels in each image from the MVTec AD dataset and then divide the images into four scale categories—*tiny*, *small*, *medium*, and *large*—based on quartile thresholds. As shown in Figure 4, MPAMA achieves performance comparable to AnomalyCLIP for tiny and small-scale anomalies, illustrating that our method does not compromise performance on small anomalies. For medium and large anomalies,

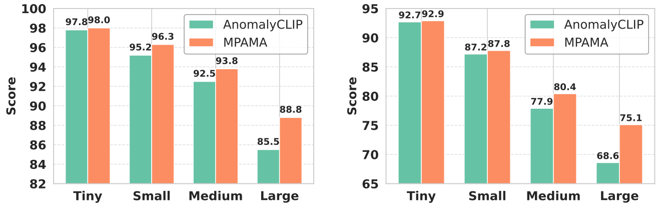

Figure 4: Scale-wise results between AnomalyCLIP and MPAMA on MVTec. **Left**: Pixel-level AUROC; **Right**: AUPRO.

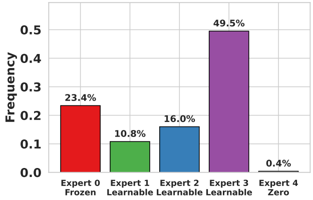

Figure 5: Frequency of expert usage on MVTec AD.

MPAMA outperforms AnomalyCLIP by a significant margin, with the performance gain increasing for larger anomalies. In summary, integrating multi-scale receptive field prompts provides an effective strategy for balancing detection across different anomaly scales while enhancing robustness to noise. More visualizations are provided in Appendix 7.

Selection frequency of Multiple Specialized Experts MPAMA leverages multiple specialized visual experts to comprehensively model the visual distribution. We analyze the frequency of expert usage across the MVTec AD dataset, as shown in Figure 5. Since some visual tokens can be well represented by the original expert, approximately 20% of tokens are routed to the frozen expert. Nearly 80% of tokens are routed to the learnable experts for adaptation, highlighting the necessity of fine-tuning beyond the frozen representation. In particular, we observe that the purple expert accounts for 50% of the routing in Figure 1(d), primarily capturing object semantics and large-scale variations. The blue expert receives 16% of the tokens, while the green expert accounts for approximately 10%. Additionally, 0.4% of tokens are routed to zero experts, indicating that very few tokens can be adequately represented by a single expert alone. It also reflects the importance of projecting tokens using multiple experts. Although all of these are learnable experts, each specializes in capturing distinct visual patterns. These demonstrate that MPAMA adaptively routes tokens to different experts based on their semantic characteristics, enabling more specialized and expressive feature modeling.

5 Ablation Study

Module Ablation We first investigate the contribution of three key modules to the overall performance of MPAMA: multi-perception text prompts (T_1), decoupled local and global text prompts (T_2), and MA (T_3). Table 3 shows that incorporating multi-perception text prompts significantly improves both image-level anomaly detection and pixel-level segmentation by capturing multi-scale anomaly semantics. When we further decouple the global and local text prompts, an additional performance gain is observed, highlighting the benefits of reducing semantic interference between coarse and fine-grained representations. Finally, after adapting the textual space, we introduce MA to dynamically route visual tokens to specialized experts. This allows MPAMA to comprehensively learn complex anomaly patterns compared to MPA.

Table 3: Ablation on proposed modules.

Module			MVTec AD		VisA	
T_1	T_2	T_3	Pixel-level	Image-level	Pixel-level	Image-level
			(91.1, 81,4)	(91.5, 96.2)	(95.5, 87.0)	(82.1, 85.4)
✓			(92.1, 86.4)	(93.0, 96.9)	(95.6, 87.5)	(83.2, 87.1)
✓	✓		(92.5, 87.5)	(94.1, 96.9)	(95.8, 87.9)	(85.0, 87.6)
✓		✓	(92.3, 86.0)	(93.1, 96.5)	(95.8, 88.1)	(84.6, 87.3)
	✓	✓	(91.4, 83.8)	(92.2, 96.3)	(95.6, 87.4)	(83.5, 86.7)
✓	✓	✓	(93.2, 88.3)	(94.5, 97.6)	(96.1, 88.6)	(85.4, 88.0)

Ablation on Perception Number In this section, we investigate the impact of varying the perception number. As shown in Table 4, increasing the number of perception levels consistently improves both image-level and pixel-level performance. The model achieves optimal performance when the perception set is 1, 2, 3, 4. However, further increasing the perception number to include a receptive field of 5 leads to a performance drop. This is due to overly large receptive fields interfering with local information modeling. Therefore, an appropriate number of perception levels is crucial for effectively capturing diverse anomaly semantics.

Table 4: Perception number ablation.

Perception	MVTec AD		VisA	
number	Pixel-level	Image-level	Pixel-level	Image-level
{1}	(92.1, 87.2)	(93.0, 96.8)	(95.7, 87.9)	(84.6, 86.9)
{1,2}	(92.3, 87.1)	(93.9, 97.3)	(95.7, 88.0)	(84.6, 87.1)
{1,2,3}	(92.3, 87.7)	(94.0, 97.5)	(95.8, 88.3)	(85.1, 87.6)
{1,2,3,4}	(93.2, 88.3)	(94.5, 97.6)	(96.1, 88.6)	(85.4, 88.0)
{1,2,3,4,5}	(92.7, 87.7)	(94.4, 97.7)	(95.8, 88.2)	(85.6, 87.9)

Ablation on Expert Number The number of experts determines model's capacity to learn specialized visual representations. As shown in Table 5, increasing the number of experts from 1 to 3 consistently improves performance on both anomaly detection and segmentation tasks. This indicates that utilizing multiple experts enables the model to capture more complex and diverse anomaly patterns.

Table 5: Expert number ablation.

Expert	MVTec AD		VisA	
number	Pixel-level	Image-level	Pixel-level	Image-level
1	(92.1, 86.4)	(93.0, 96.9)	(95.6, 87.5)	(83.2, 87.1)
2	(92.3, 87.0)	(93.0, 97.1)	(95.8, 87.8)	(84.1, 87.5)
3	(92.8, 87.8)	(94.1, 97.3)	(96.0, 88.1)	(85.0, 87.8)
4	(93.2, 88.3)	(94.5, 97.6)	(96.1, 88.4)	(85.1, 88.0)
5	(93.0, 87.9)	(94.6, 97.8)	(96.1, 88.6)	(85.4, 88.0)
6	(92.9, 87.9)	(94.7, 97.8)	(96.2, 88.3)	(85.3, 87.9)

However, when the number of experts increases to 6, the performance improvement becomes marginal compared to using 4 or 5 experts. Hence, an appropriate number of experts improves the learning of anomaly patterns during model training on the auxiliary dataset.

6 Related Work

Zero-shot Anomaly Detection Recently, zero-shot anomaly detection (ZSAD) has emerged as an active research area, attracting increasing attention from AD community (Aota et al., 2023; Liznerski et al., 2022; Esmaeilpour et al., 2022; Zhou et al., 2024a; Chen et al., 2023; Zhou et al., 2024b). A promising research line is to leverage CLIP as the backbone for ZSAD (Jeong et al., 2023; Chen et al., 2023; Zhou et al., 2024a). WinCLIP designs human-crafted normal and abnormal text prompts for zero-shot anomaly detection without fine-tuning. AnomalyCLIP (Zhou et al., 2024a) proposes object-agnostic prompt learning and demonstrates strong potential across diverse domains. Subsequent methods enhance performance via ensemble prompt strategies for modeling more anomaly semantics such as FAprompt (ZHU et al., 2025) and BayesCLIP (Qu et al., 2025), or integrate visual adaptation techniques to refine the alignment between visual and textual features such as VCP-CLIP (Qu et al., 2024), AdaptCLIP (Cao et al., 2024), and AA-CLIP (Ma et al., 2025). However, most methods rely on single-scale text embeddings and coupled alignment strategies. This coarse alignment hinders the model's ability to capture the inherently multi-scale nature of anomalies. Our approach introduces multi-perception prompt learning, which assigns varied receptive fields to text prompts. Combined with a fine-grained expert assignment mechanism, this enables precise anomaly detection across multiple spatial scales. MLLM-based methods (Li et al., 2023; Gu et al., 2024b; Xu et al., 2025) demonstrate that fine-tuned MLLMs can perform basic reasoning on detected anomalies. However, these approaches require significantly larger backbones and substantially more training data.

Prompt Learning in Anomaly Detection Prompt learning aims to achieve lightweight domain adaptation with minimal training overhead by updating only a small set of trainable parameters. CoOp (Zhou et al., 2022b;a) first introduced this approach in the context of few-shot classification by learning task-specific prompts for CLIP. AnomalyCLIP (Zhou et al., 2024a) was the first to extend prompt learning to anomaly detection. It introduces object-agnostic prompt tuning to discard explicit class semantics, promoting more generalized anomaly representations. PromptAD (Li et al., 2024), FILo (Gu et al., 2024a), and BayesCLIP (Qu et al., 2025) propose hybrid prompts that combine learnable text embeddings with prior textual knowledge. However, existing methods typically employ a single-scale text prompt to model both fine-grained local anomalies and high-level global semantics. In contrast, we identify that such a coupled single-scale prompt is insufficient for capturing the diverse nature of anomaly semantics. To address this, we propose multi-perception text prompts, which assign diverse receptive fields to different prompts. Furthermore, we disentangle local and global anomaly modeling and enable more comprehensive anomaly semantics.

7 Conclusion

In this paper, we identify two key shortcomings in existing CLIP-based approaches stemming from single-level alignment. To address these challenges, we enhance visual-textual representations by extending single-level alignment to multi-level alignment. Specifically, we propose a multi-granularity alignment framework that strengthens cross-modal alignment: Multi-perception alignment enriches the textual space by attaching prompts with diverse receptive fields; MoE adaptation dynamically routes visual tokens to multiple specialized experts, enabling multi-granularity, token-wise representation. Based on this framework, we develop two models, MPA and MPAMA, capable of capturing rich and multi-granularity anomaly semantics. Extensive experiments on standard benchmarks demonstrate the superior performance of our approaches.

Limitations While MPAMA achieves strong performance through multiple specialized experts, this design can lead to increased computational overhead as the number of experts grows. However, the additional cost remains low in practice, since only two experts are activated per token during inference. A detailed analysis of memory consumption is provided in Appendix C.

Broader Impacts This paper proposes a new perspective on fine-tuning vision-language models that is fully compliant with legal and regulatory guidelines. While current prompt-learning methods typically rely on single-level alignment, our approach introduces a multi-level alignment strategy capable of capturing structural semantics more effectively. We hope this work draws greater attention to the role of receptive fields in the adaptation of vision-language models.

Reproducibility statement

We provide dataset details in Appendix A and baseline descriptions in Appendix B. Further analyses are included in the following appendices: computational overhead in Appendix C, prompt design strategies in Appendix E, weight coefficient sensitivity in Appendix F, and perception level ablation in Appendix G. To offer a deeper understanding of MPAMA's behavior, failure cases are presented in Appendix H. Additionally, subset-level quantitative results and visualizations are provided in Appendix I. **The code will be made available once accepted.**

References

Toshimichi Aota, Lloyd Teh Tzer Tong, and Takayuki Okatani. Zero-shot versus many-shot: Unsupervised texture anomaly detection. In *Proceedings of the IEEE/CVF Winter Conference on Applications of Computer Vision*, pp. 5564–5572, 2023.

Paul Bergmann, Michael Fauser, David Sattlegger, and Carsten Steger. Mvtec ad–a comprehensive real-world dataset for unsupervised anomaly detection. In *Proceedings of the IEEE/CVF conference on computer vision and pattern recognition*, pp. 9592–9600, 2019.

Paul Bergmann, Michael Fauser, David Sattlegger, and Carsten Steger. Uninformed students: Student-teacher anomaly detection with discriminative latent embeddings. In *Proceedings of the IEEE/CVF conference on computer vision and pattern recognition*, pp. 4183–4192, 2020.

Jorge Bernal, F Javier Sánchez, Gloria Fernández-Esparrach, Debora Gil, Cristina Rodríguez, and Fernando Vilariño. Wm-dova maps for accurate polyp highlighting in colonoscopy: Validation vs. saliency maps from physicians. *Computerized medical imaging and graphics*, 43:99–111, 2015.

Yunkang Cao, Jiangning Zhang, Luca Frittoli, Yuqi Cheng, Weiming Shen, and Giacomo Boracchi. Adaclip: Adapting clip with hybrid learnable prompts for zero-shot anomaly detection. In *European Conference on Computer Vision*, pp. 55–72. Springer, 2024.

Xuhai Chen, Yue Han, and Jiangning Zhang. A zero-/few-shot anomaly classification and segmentation method for cvpr 2023 vand workshop challenge tracks 1&2: 1st place on zero-shot ad and 4th place on few-shot ad. *arXiv preprint arXiv:2305.17382*, 2023.

Yuanhong Chen, Yu Tian, Guansong Pang, and Gustavo Carneiro. Deep one-class classification via interpolated gaussian descriptor. In *Proceedings of the AAAI Conference on Artificial Intelligence*, volume 36, pp. 383–392, 2022.

Choubo Ding, Guansong Pang, and Chunhua Shen. Catching both gray and black swans: Open-set supervised anomaly detection. In *Proceedings of the IEEE/CVF Conference on Computer Vision and Pattern Recognition*, pp. 7388–7398, 2022.

Sepideh Esmaeilpour, Bing Liu, Eric Robertson, and Lei Shu. Zero-shot out-of-distribution detection based on the pre-trained model clip. In *Proceedings of the AAAI conference on artificial intelligence*, volume 36, pp. 6568–6576, 2022.

Bin-Bin Gao. MetaUAS: Universal anomaly segmentation with one-prompt meta-learning. In *The Thirty-eighth Annual Conference on Neural Information Processing Systems*, 2024. URL `https://openreview.net/forum?id=4jegYnUMHb`.

Zhaopeng Gu, Bingke Zhu, Guibo Zhu, Yingying Chen, Hao Li, Ming Tang, and Jinqiao Wang. Filo: Zero-shot anomaly detection by fine-grained description and high-quality localization. In *Proceedings of the 32nd ACM International Conference on Multimedia*, pp. 2041–2049, 2024a.

Zhaopeng Gu, Bingke Zhu, Guibo Zhu, Yingying Chen, Ming Tang, and Jinqiao Wang. Anomalygpt: Detecting industrial anomalies using large vision-language models. In *Proceedings of the AAAI conference on artificial intelligence*, volume 38, pp. 1932–1940, 2024b.

David Gutman, Noel C. F. Codella, Emre Celebi, Brian Helba, Michael Marchetti, Nabin Mishra, and Allan Halpern. Skin lesion analysis toward melanoma detection: A challenge at the international symposium on biomedical imaging (isbi) 2016, hosted by the international skin imaging collaboration (isic), 2016.

A. Hamada. Br35h: Brain tumor detection 2020. *Online. Available: https://www.kaggle.com/datasets/ahmedhamada0/brain-tumor-detection*, 2020.

Steven A Hicks, Debesh Jha, Vajira Thambawita, Pål Halvorsen, Hugo L Hammer, and Michael A Riegler. The endotect 2020 challenge: evaluation and comparison of classification, segmentation and inference time for endoscopy. In *Pattern Recognition. ICPR International Workshops and Challenges: Virtual Event, January 10-15, 2021, Proceedings, Part VIII*, pp. 263–274. Springer, 2021.

Chaoqin Huang, Haoyan Guan, Aofan Jiang, Ya Zhang, Michael Spratling, and Yan-Feng Wang. Registration based few-shot anomaly detection. In *European Conference on Computer Vision*, pp. 303–319. Springer, 2022.

Jongheon Jeong, Yang Zou, Taewan Kim, Dongqing Zhang, Avinash Ravichandran, and Onkar Dabeer. Winclip: Zero-/few-shot anomaly classification and segmentation. In *Proceedings of the IEEE/CVF Conference on Computer Vision and Pattern Recognition*, pp. 19606–19616, 2023.

Stepan Jezek, Martin Jonak, Radim Burget, Pavel Dvorak, and Milos Skotak. Deep learning-based defect detection of metal parts: evaluating current methods in complex conditions. In *2021 13th International congress on ultra modern telecommunications and control systems and workshops (ICUMT)*, pp. 66–71. IEEE, 2021.

Debesh Jha, Pia H Smedsrud, Michael A Riegler, Pål Halvorsen, Thomas de Lange, Dag Johansen, and Håvard D Johansen. Kvasir-seg: A segmented polyp dataset. In *MultiMedia Modeling: 26th International Conference, MMM 2020, Daejeon, South Korea, January 5–8, 2020, Proceedings, Part II 26*, pp. 451–462. Springer, 2020.

Dmitry Lepikhin, HyoukJoong Lee, Yuanzhong Xu, Dehao Chen, Orhan Firat, Yanping Huang, Maxim Krikun, Noam Shazeer, and Zhifeng Chen. {GS}hard: Scaling giant models with conditional computation and automatic sharding. In *International Conference on Learning Representations*, 2021. URL `https://openreview.net/forum?id=qrwe7XHTmYb`.

Xiaoya Li, Xiaofei Sun, Yuxian Meng, Junjun Liang, Fei Wu, and Jiwei Li. Dice loss for data-imbalanced nlp tasks. *arXiv preprint arXiv:1911.02855*, 2019.

Yiting Li, Adam David Goodge, Fayao Liu, and Chuan-Sheng Foo. Promptad: Zero-shot anomaly detection using text prompts. *2024 IEEE/CVF Winter Conference on Applications of Computer Vision (WACV)*, pp. 1082–1091, 2024. URL `https://api.semanticscholar.org/CorpusID:267755280`.

Yuanze Li, Haolin Wang, Shihao Yuan, Ming Liu, Debin Zhao, Yiwen Guo, Chen Xu, Guangming Shi, and Wangmeng Zuo. Myriad: Large multimodal model by applying vision experts for industrial anomaly detection. *ArXiv*, abs/2310.19070, 2023. URL `https://api.semanticscholar.org/CorpusID:264817610`.

Tsung-Yi Lin, Priya Goyal, Ross Girshick, Kaiming He, and Piotr Dollár. Focal loss for dense object detection. In *Proceedings of the IEEE international conference on computer vision*, pp. 2980–2988, 2017.

Jie Liu, Yixiao Zhang, Jie-Neng Chen, Junfei Xiao, Yongyi Lu, Bennett A Landman, Yixuan Yuan, Alan Yuille, Yucheng Tang, and Zongwei Zhou. Clip-driven universal model for organ segmentation and tumor detection. In *Proceedings of the IEEE/CVF international conference on computer vision*, pp. 21152–21164, 2023.

Philipp Liznerski, Lukas Ruff, Robert A. Vandermeulen, Billy Joe Franks, Marius Kloft, and Klaus Robert Muller. Explainable deep one-class classification. In *International Conference on Learning Representations*, 2021. URL `https://openreview.net/forum?id=A5VV3UyIQz`.

Philipp Liznerski, Lukas Ruff, Robert A. Vandermeulen, Billy Joe Franks, Klaus Robert Muller, and Marius Kloft. Exposing outlier exposure: What can be learned from few, one, and zero outlier images. *Transactions on Machine Learning Research*, 2022. ISSN 2835-8856. URL `https://openreview.net/forum?id=3v78awEzyB`.

Wenxin Ma, Xu Zhang, Qingsong Yao, Fenghe Tang, Chenxu Wu, Yingtai Li, Rui Yan, Zihang Jiang, and S.Kevin Zhou. Aa-clip: Enhancing zero-shot anomaly detection via anomaly-aware clip. *ArXiv*, abs/2503.06661, 2025. URL `https://api.semanticscholar.org/CorpusID:276902786`.

Pankaj Mishra, Riccardo Verk, Daniele Fornasier, Claudio Piciarelli, and Gian Luca Foresti. Vt-adl: A vision transformer network for image anomaly detection and localization. In *2021 IEEE 30th International Symposium on Industrial Electronics (ISIE)*, pp. 01–06. IEEE, 2021.

Guansong Pang, Choubo Ding, Chunhua Shen, and Anton van den Hengel. Explainable deep few-shot anomaly detection with deviation networks. *arXiv preprint arXiv:2108.00462*, 2021.

Ziyuan Qin, Huahui Yi, Qicheng Lao, and Kang Li. MEDICAL IMAGE UNDERSTANDING WITH PRETRAINED VISION LANGUAGE MODELS: A COMPREHENSIVE STUDY. In *The Eleventh International Conference on Learning Representations*, 2023. URL `https://openreview.net/forum?id=txlWziuCE5W`.

Zhen Qu, Xian Tao, Mukesh Prasad, Fei Shen, Zhengtao Zhang, Xinyi Gong, and Guiguang Ding. Vcp-clip: A visual context prompting model for zero-shot anomaly segmentation. In *European Conference on Computer Vision*, 2024. URL `https://api.semanticscholar.org/CorpusID:271244532`.

Zhen Qu, Xian Tao, Xinyi Gong, Shichen Qu, Qiyu Chen, Zhengtao Zhang, Xingang Wang, and Guiguang Ding. Bayesian prompt flow learning for zero-shot anomaly detection. In *Proceedings of the Computer Vision and Pattern Recognition Conference*, pp. 30398–30408, 2025.

Alec Radford, Jong Wook Kim, Chris Hallacy, Aditya Ramesh, Gabriel Goh, Sandhini Agarwal, Girish Sastry, Amanda Askell, Pamela Mishkin, Jack Clark, et al. Learning transferable visual models from natural language supervision. In *International conference on machine learning*, pp. 8748–8763. PMLR, 2021.

Mohammadreza Salehi, Niousha Sadjadi, Soroosh Baselizadeh, Mohammad H Rohban, and Hamid R Rabiee. Multiresolution knowledge distillation for anomaly detection. In *Proceedings of the IEEE/CVF conference on computer vision and pattern recognition*, pp. 14902–14912, 2021.

Domen Tabernik, Samo Šela, Jure Skvarč, and Danijel Skočaj. Segmentation-based deep-learning approach for surface-defect detection. *Journal of Intelligent Manufacturing*, 31(3):759–776, 2020.

Nima Tajbakhsh, Suryakanth R Gurudu, and Jianming Liang. Automated polyp detection in colonoscopy videos using shape and context information. *IEEE transactions on medical imaging*, 35(2):630–644, 2015.

Matthias Wieler and Tobias Hahn. Weakly supervised learning for industrial optical inspection. In *DAGM symposium in*, volume 6, 2007.

Guoyang Xie, Jingbao Wang, Jiaqi Liu, Feng Zheng, and Yaochu Jin. Pushing the limits of fewshot anomaly detection in industry vision: Graphcore. *arXiv preprint arXiv:2301.12082*, 2023.

Jiacong Xu, Shao-Yuan Lo, Bardia Safaei, Vishal M Patel, and Isht Dwivedi. Towards zero-shot anomaly detection and reasoning with multimodal large language models. In *Proceedings of the Computer Vision and Pattern Recognition Conference*, pp. 20370–20382, 2025.

Zhiyuan You, Lei Cui, Yujun Shen, Kai Yang, Xin Lu, Yu Zheng, and Xinyi Le. A unified model for multi-class anomaly detection. *Advances in Neural Information Processing Systems*, 35: 4571–4584, 2022.

Kaiyang Zhou, Jingkang Yang, Chen Change Loy, and Ziwei Liu. Conditional prompt learning for vision-language models. In *Proceedings of the IEEE/CVF Conference on Computer Vision and Pattern Recognition*, pp. 16816–16825, 2022a.

Kaiyang Zhou, Jingkang Yang, Chen Change Loy, and Ziwei Liu. Learning to prompt for vision-language models. *International Journal of Computer Vision*, 130(9):2337–2348, 2022b.

Qihang Zhou, Guansong Pang, Yu Tian, Shibo He, and Jiming Chen. AnomalyCLIP: Object-agnostic prompt learning for zero-shot anomaly detection. In *The Twelfth International Conference on Learning Representations*, 2024a. URL `https://openreview.net/forum?id=buC4E91xZE`.

Qihang Zhou, Jiangtao Yan, Shibo He, Wenchao Meng, and Jiming Chen. PointAD: Comprehending 3d anomalies from points and pixels for zero-shot 3d anomaly detection. In *The Thirty-eighth Annual Conference on Neural Information Processing Systems*, 2024b. URL `https://openreview.net/forum?id=02CIZ8qeDc`.

JIAWEN ZHU, Yew-Soon Ong, Chunhua Shen, and Guansong Pang. Fine-grained abnormality prompt learning for zero-shot anomaly detection, 2025. URL `https://openreview.net/forum?id=kS27PPs3yR`.

Yang Zou, Jongheon Jeong, Latha Pemula, Dongqing Zhang, and Onkar Dabeer. Spot-the-difference self-supervised pre-training for anomaly detection and segmentation. In *European Conference on Computer Vision*, pp. 392–408. Springer, 2022.

A Datasets

In this section, we present the statistical summary of the datasets used in our study. The 15 datasets span both industrial and medical domains. The details are reported in Table A.

Table 6: Overview of datasets used for anomaly and disease detection across industrial and medical domains.

Dataset	**Domain**	**Modality**	$\lvert\mathcal{C}\rvert$	**Normal / Anomalous**	**Application**
			Industrial Inspection		
MVTec AD	Object & Texture	RGB	15	(467, 1258)	Defect detection
VisA	Object	RGB	12	(962, 1200)	Defect detection
MPDD	Object	RGB	6	(176, 282)	Defect detection
BTAD	Object	RGB	3	(451, 290)	Defect detection
SDD	Object	RGB	1	(181, 74)	Defect detection
DAGM	Texture	RGB	10	(6996, 1054)	Defect detection
DTD-Synthetic	Texture	RGB	12	(357, 947)	Defect detection
			Skin Lesion Analysis		
ISIC	Skin	RGB	1	(0, 379)	Skin cancer detection
			Colon Polyp Detection		
ClinicDB	Colon	Endoscopy	1	(0, 612)	Polyp detection
ColonDB	Colon	Endoscopy	1	(0, 380)	Polyp detection
Kvasir	Colon	Endoscopy	1	(0, 1000)	Polyp detection
Endo	Colon	Endoscopy	1	(0, 200)	Polyp detection
			Thyroid Nodule Detection		
			Brain Tumor Detection		
HeadCT	Brain	CT	1	(100, 100)	Tumor detection
BrainMRI	Brain	MRI	1	(98, 155)	Tumor detection
Br35H	Brain	MRI	1	(1500, 1500)	Tumor detection

B Baselines

To comprehensively evaluate the performance of our model, we benchmark it against a range of ZSAD approaches. **We exclude the approaches based on large multimodal models (Gu et al., 2024b; Xu et al., 2025; Li et al., 2023) from comparison due to their use of stronger backbones and substantially more data**. We compare our method with SOTA ZSAD approaches, WinCLIP (Jeong et al., 2023), VAND (Chen et al., 2023), AnomalyCLIP (Zhou et al., 2024a), AdaCLIP (Cao et al.,

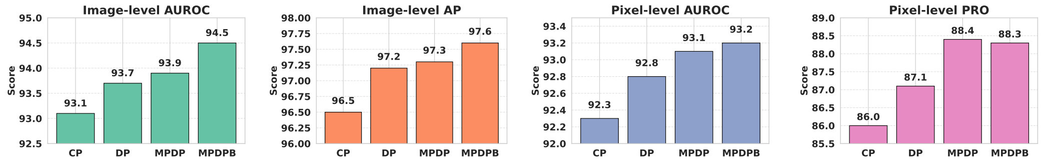

(a) Image-level AUROC. (b) Image-level AP. (c) Pixel-level AUROC. (d) PRO.

Figure 6: Comparison using different text prompts. We denote coupling prompt, decoupling prompt, multi-perception prompt, and multi-perception prompt with cross bridge as CP, DP, MPDP, and MPDPB, respectively.

2024), and FAprompt (ZHU et al., 2025). Below is an overview of the compared approaches and the strategies used for adaptation:

- **WinCLIP (CVPR 2023)** (Jeong et al., 2023): A leading framework for zero-shot anomaly segmentation that introduces a rich set of prompts crafted for anomaly scenarios. It further integrates a window-based scaling mechanism to improve localization precision. All experimental settings replicate those reported in the original paper.

- **VAND (ARXIV 2023)** (Chen et al., 2023): VAND refines the prompt design and introduces learnable linear transformations to better capture fine-grained visual details. We adopt the original configuration to ensure comparability with reported results.

- **AdaCLIP (ECCV 2024)** (Cao et al., 2024): AdaCLIP uses the human-crafted text prompts as the text embedding, and instead adapts the visual space for ZSAD.

- **AnomalyCLP (ICLR 2024)** (Zhou et al., 2022b): AnomalyCLIP introduces an object-agnostic prompt learning framework to enhance generalization across diverse anomaly types. In addition, it integrates a DPAM to refine visual feature space of CLIP for more precise detection and segmentation

- **FAPromt (ICCV 2025)** (ZHU et al., 2025): FAPrompt ensembles multiple learnable text prompts to learn the comprehensive anomaly semantics.

C Computation Overhead

Table 7: Analysis of computation overhead.

Methods	Inference Time (s)	FPS	Peak GPU Memory (MB)	MVTec AD		VisA	
				pixel-level	image-level	pixel-level	image-level
AnomalyCLIP	0.124	8.04	2235MB	(91.1, 81,4)	(91.5, 96.2)	(95.5, 87.0)	(82.1, 85.4)
MPA	0.137	7.29	3275MB	(92.5, 87.5)	(94.1, 96.9)	(95.8, 87.9)	(85.0, 87.6)
MPAMA	0.152	6.56	3275MB	(93.2, 88.3)	(94.5, 97.6)	(96.1, 88.6)	(85.4, 88.0)

Besides accuracy, computational overhead is also a crucial metric for evaluating the performance of anomaly detection algorithms. In this section, we investigate whether MPAMA can effectively balance detection performance and computational cost. To this end, we measure GPU memory consumption during training and inference speed in terms of FPS. All experiments are conducted on an idle NVIDIA A100 GPU with a batch size of 1. The results are summarized in Table 7. Compared to AnomalyCLIP, both MPA and MPAMA incur slightly higher inference time and GPU memory usage. Specifically, the inference time of AnomalyCLIP and MPAMA is 0.124s and 0.152s, respectively. Despite this negligible increase in inference time, our method achieves notable improvements in anomaly detection and segmentation performance.

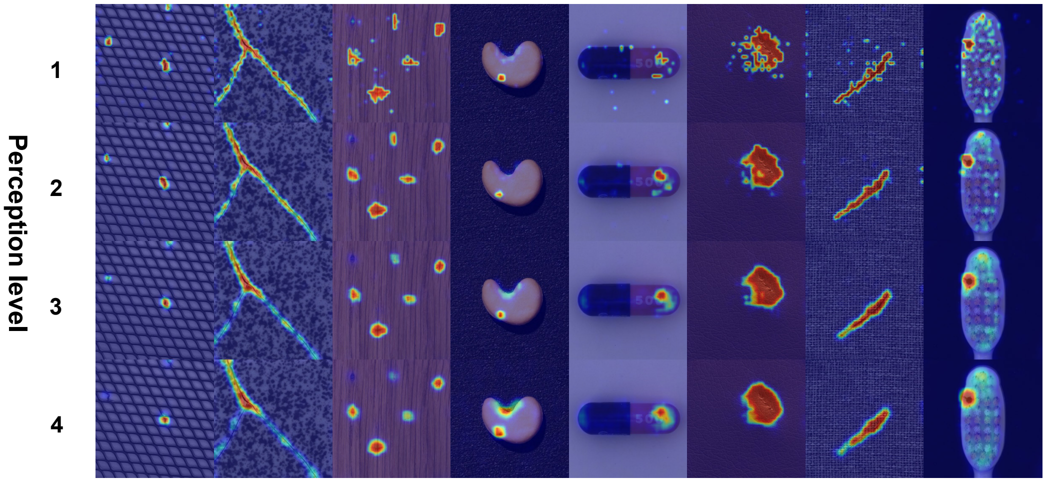

Figure 7: Visualization results using text prompts with varying receptive fields. From top to bottom, the receptive field size increases from 1 to 4.

D VISUALIZATION WITH DIFFERENT PERCEPTION LEVELS.

E ANALYSIS OF DIFFERENT PROMPT STRATEGIES.

Here, we analyze the effect of using different types of text prompts. We explore four configurations: Coupling Prompt (CP), which uses a single text prompt to jointly model both local and global semantics; Decoupling Prompt (DP), which uses two independent prompts to separately model global and local semantics; Multi-Perception Decoupling Prompt (MPDP), which extends DP by assigning a unique, unshared prompt to each perception scale; and Multi-Perception Decoupling Prompt with Bridge (MPDPB), which further introduces a cross-bridge mechanism to incorporate salient local semantic features into the global context. All variants are optimized using the same loss function described in Equ. 5 and Equ. 6. As shown in Figure 6, DP provides a consistent improvement across both image-level and pixel-level metrics, indicating that fully coupling global and local prompts hinders accurate anomaly modeling. MPDP takes this further by decoupling the local prompt across multiple perception scales. This further decoupling benefits pixel-level detection. Finally, MPDPB enhances global semantic modeling by integrating salient local features through the cross-bridge, leading to gains in image-level metrics.

F HYPERPARAMETER ABLATION

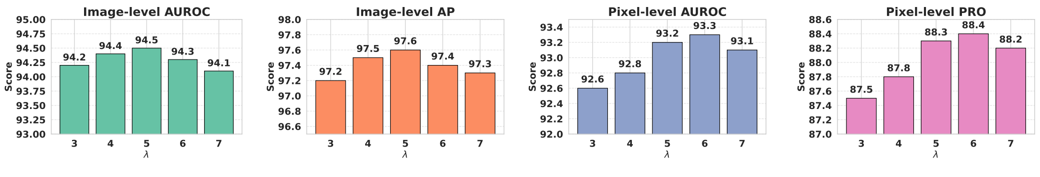

(a) Image-level AUROC. (b) Image-level AP. (c) Pixel-level AUROC. (d) PRO.

Figure 8: The effect of λ

Here, we investigate the effect of the coefficient λ on the model's performance. We set $\lambda \in \{3, 4, 5, 6, 7\}$. As shown in Figure 8, increasing λ initially improves both image-level and pixel-level performance. However, as λ continues to increase, performance begins to decline. Empirically, $\lambda = 5$ achieves a good balance between image-level and pixel-level performance.

Table 8: Ablation study on perception level.

Perception level	MVTec AD		VisA	
	Pixel-level	Image-level	Pixel-level	Image-level
{1,2,3,4}	(93.2, 88.3)	(94.5, 97.6)	(96.1, 88.6)	(85.4, 88.0)
{2,3,4,5}	(92.8, 87.5)	(94.4, 97.7)	(95.9, 88.0)	(85.1, 87.6)
{3,4,5,6}	(92.3, 86.1)	(94.3, 97.1)	(95.7, 87.5)	(84.6, 86.8)

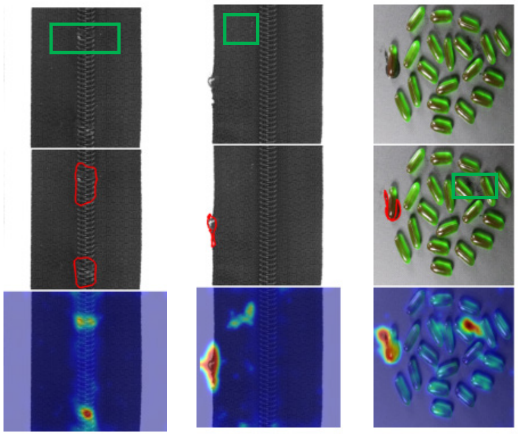

Figure 9: Illustration of false detection cases. Misdetected regions are marked with green squares.

G Ablation on Perception Level

We further explore the influence of the perception scale while keeping the number of perception levels fixed. As shown in Table 8, the configuration $\{1, 2, 3, 4\}$ achieves the best performance compared to alternatives such as $\{2, 3, 4, 5\}$ and $\{3, 4, 5, 6\}$. These results highlight that small-scale perception (i.e., receptive field 1) is crucial for fine-grained anomaly detection. In contrast, incorporating excessively large receptive fields can degrade performance due to detailed information loss.

H Failure Case

Although MPAMA demonstrates promising performance across a wide range of objects, it is crucial to examine its failure cases to gain deeper insights into its behavior and limitations. To this end, we present visualizations of false detections in Figure 9. In the 'zipper' category, the regions highlighted with green squares indicate surface flaws that are not annotated as anomalies in the ground truth. A similar phenomenon is observed with subtle fabric defects near the zipper, which are visually abnormal yet unlabeled. Furthermore, MPAMA occasionally misinterprets background artifacts as anomalies. The third column displays several capsules placed on a desk with a visible black stain. Although the stain may appear anomalous, the annotation only focuses exclusively on object anomalies. This raises an important research question: How can we guide MPAMA to focus specifically on object-centric anomalies while disregarding irrelevant background artifacts?

I Visualization on Category-wise Segmentation

Category-wise visualizations are provided to facilitate an intuitive understanding of MPAMA's detection performance.

Table 9: Subset-level performance comparison (AUROC) for anomaly segmentation on MVTec AD.

Object name	**WinCLIP**	**VAND**	**AnomalyCLIP**	**MPL**	**MPAMA**
Carpet	95.4	98.4	98.8	99.2	99.5
Bottle	89.5	83.4	90.4	91.9	93.5
Hazelnut	94.3	96.1	97.1	97.3	97.2
Leather	96.7	99.1	98.6	99.0	99.2
Cable	77.0	72.3	78.9	82.7	84.7
Capsule	86.9	92.0	95.8	97.1	97.1
Grid	82.2	95.8	97.3	98.2	98.2
Pill	80.0	76.2	92.0	93.1	93.9
Transistor	74.7	62.4	71.0	71.3	74.0
Metal_nut	61.0	65.4	74.4	72.0	75.2
Screw	89.6	97.8	97.5	97.4	98.1
Toothbrush	86.9	95.8	91.9	94.7	96.1
Zipper	91.6	91.1	91.4	96.7	97.9
Tile	77.6	92.7	94.6	97.7	97.1
Wood	93.4	95.8	96.5	98.0	98.0
Mean	85.1	87.6	91.1	92.5	93.2

Table 10: Subset-level performance comparison (PRO) for anomaly segmentation on MVTec AD.

Object name	**WinCLIP**	**VAND**	**AnomalyCLIP**	**MPL**	**MPAMA**
Carpet	84.1	48.5	90.1	97.5	96.4
Bottle	76.4	45.6	80.9	84.3	85.6
Hazelnut	81.6	70.3	92.4	91.1	92.1
Leather	91.1	72.4	92.2	98.0	98.0
Cable	42.9	25.7	64.4	74.7	78.5
Capsule	62.1	51.3	87.2	93.5	94.8
Grid	57.0	31.6	75.6	93.0	91.5
Pill	65.0	65.4	88.2	93.2	94.5
Transistor	43.4	21.3	58.1	55.6	57.1
Metal_nut	31.8	38.4	71.0	72.7	76.9
Screw	68.5	67.1	88.0	89.1	89.9
Toothbrush	67.7	54.5	88.5	92.1	92.4
Zipper	71.7	10.7	65.3	89.0	91.6
Tile	51.2	26.7	87.6	94.3	90.1
Wood	74.1	31.1	91.2	94.9	94.7
Mean	64.6	44.0	81.4	87.5	88.3

Table 11: Subset-level performance comparison (AUROC) for anomaly classification on MVTec AD.

Object name	**WinCLIP**	**VAND**	**AnomalyCLIP**	**MPL**	**MPAMA**
Carpet	100.0	99.5	100.0	99.7	100.0
Bottle	99.2	92.0	89.3	92.5	92.9
Hazelnut	93.9	89.6	97.2	94.6	94.5
Leather	100.0	99.7	99.8	99.9	99.7
Cable	86.5	88.4	69.8	94.3	94.4
Capsule	72.9	79.9	89.9	95.6	96.5
Grid	98.8	86.3	97.0	98.9	99.3
Pill	79.1	80.5	81.8	88.4	87.6
Transistor	88.0	80.8	92.8	89.4	89.5
Metal_nut	97.1	68.4	93.6	81.7	85.6
Screw	83.3	84.9	81.1	84.0	84.5
Toothbrush	88.0	53.8	84.7	96.8	96.8
Zipper	91.5	89.6	98.5	99.7	98.8
Tile	100.0	99.9	100.0	98.7	98.7
Wood	99.4	99.0	96.8	98.1	97.8
Mean	91.8	86.1	91.5	94.1	94.5

Table 12: Subset-level performance comparison (AP) for anomaly classification on MVTec AD.

Object name	**WinCLIP**	**VAND**	**AnomalyCLIP**	**MPL**	**MPAMA**
Carpet	100.0	99.8	100.0	99.9	100.0
Bottle	99.8	97.7	97.0	97.7	98.0
Hazelnut	96.9	94.8	98.6	97.2	96.9
Leather	100.0	99.9	99.9	99.9	99.9
Cable	91.2	93.1	81.4	96.7	96.4
Capsule	91.5	95.5	97.9	99.0	99.4
Grid	99.6	94.9	99.1	99.7	99.5
Pill	95.7	96.0	95.4	97.5	97.4
Transistor	87.1	77.5	90.6	88.4	88.9
Metal_nut	99.3	91.9	98.5	95.7	96.6
Screw	93.1	93.6	92.5	93.5	94.0
Toothbrush	95.6	71.5	93.7	98.6	98.6
Zipper	97.5	97.1	99.6	99.8	99.6
Tile	100.0	100.0	100.0	99.6	99.5
Wood	99.8	99.7	99.2	99.4	99.3
Mean	96.5	93.5	96.2	96.9	97.6

Table 13: Subset-level performance comparison (AUROC) for anomaly segmentation on VisA.

Object name	**WinCLIP**	**VAND**	**AnomalyCLIP**	**MPL**	**MPAMA**
Candle	88.9	97.8	98.8	98.5	98.6
Capsules	81.6	97.5	95.0	94.6	95.8
Cashew	84.7	86.0	93.8	95.3	95.5
Chewinggum	93.3	99.5	99.3	99.1	99.6
Fryum	88.5	92.0	94.6	94.8	95.0
Macaroni1	70.9	98.8	98.3	98.6	99.0
Macaroni2	59.3	97.8	97.6	97.4	97.6
Pcb1	61.2	92.7	94.1	95.0	96.7
Pcb2	71.6	89.7	92.4	92.9	92.8
Pcb3	85.3	88.4	88.4	88.6	87.7
Pcb4	94.4	94.6	95.7	96.7	96.7
Pipe_fryum	75.4	96.0	98.2	98.4	98.4
Mean	79.6	94.2	95.5	95.8	96.1

Table 14: Subset-level performance comparison (PRO) for anomaly segmentation on VisA.

Object name	**WinCLIP**	**VAND**	**AnomalyCLIP**	**MPL**	**MPAMA**
Candle	83.5	92.5	96.2	95.1	95.3
Capsules	35.3	86.7	78.5	80.2	84.9
Cashew	76.4	91.7	91.6	92.3	93.3
Chewinggum	70.4	87.3	91.2	92.7	90.7
Fryum	77.4	89.7	86.8	83.9	85.3
Macaroni1	34.3	93.2	89.8	93.6	94.4
Macaroni2	21.4	82.3	84.2	87.3	85.7
Pcb1	26.3	87.5	81.7	83.7	88.2
Pcb2	37.2	75.6	78.9	81.3	81.8
Pcb3	56.1	77.8	77.1	76.4	76.6
Pcb4	80.4	86.8	91.3	91.6	91.5
Pipe_fryum	82.3	90.9	96.8	96.5	95.4
Mean	56.8	86.8	87.0	87.9	88.6

Table 15: Subset-level performance comparison (AUROC) for anomaly classification on VisA.

Object name	**WinCLIP**	**VAND**	**AnomalyCLIP**	**MPL**	**MPAMA**
Candle	95.4	83.8	79.3	85.2	83.5
Capsules	85.0	61.2	81.5	90.5	89.8
Cashew	92.1	87.3	76.3	90.4	90.8
Chewinggum	96.5	96.4	97.4	97.6	97.2
Fryum	80.3	94.3	93.0	92.2	92.7
Macaroni1	76.2	71.6	87.2	86.2	87.4
Macaroni2	63.7	64.6	73.4	75.2	76.3
Pcb1	73.6	53.4	85.4	75.9	76.4
Pcb2	51.2	71.8	62.2	66.0	68.8
Pcb3	73.4	66.8	62.7	66.7	68.2
Pcb4	79.6	95.0	93.9	97.8	98.0
Pipe_fryum	69.7	89.9	92.4	96.0	96.2
Mean	78.1	78.0	82.1	85.0	85.4

Table 16: Subset-level performance comparison (AP) for anomaly classification on VisA.

Object name	**WinCLIP**	**VAND**	**AnomalyCLIP**	**MPL**	**MPAMA**
Candle	95.8	86.9	81.1	87.9	86.4
Capsules	90.9	74.3	88.7	94.8	94.7
Cashew	96.4	94.1	89.4	95.7	95.7
Chewinggum	98.6	98.4	98.9	98.8	99.0
Fryum	90.1	97.2	96.8	96.1	96.5
Macaroni1	75.8	70.9	86.0	87.1	88.4
Macaroni2	60.3	63.2	72.1	74.9	76.6
Pcb1	78.4	57.2	87.0	78.8	78.6
Pcb2	49.2	73.8	64.3	68.5	71.1
Pcb3	76.5	70.7	70.0	73.1	73.1
Pcb4	77.7	95.1	94.4	97.4	97.7
Pipe_fryum	82.3	94.8	96.3	97.8	98.5
Mean	81.2	81.4	85.4	87.6	88.0

Table 17: Subset-level performance comparison (AUROC) for anomaly segmentation on MPDD.

Object name	**WinCLIP**	**VAND**	**AnomalyCLIP**	**MPL**	**MPAMA**
Bracket_black	57.8	96.3	95.7	96.4	97.0
Bracket_brown	72.2	86.2	94.4	94.5	95.2
Bracket_white	79.5	99.0	99.8	99.4	100.0
Connector	79.0	90.6	97.2	96.9	97.3
Metal_plate	92.6	93.1	93.8	94.7	93.6
Tubes	77.6	99.1	98.1	96.9	97.6
Mean	76.4	94.1	96.5	96.5	96.8

Table 18: Subset-level performance comparison (PRO) for anomaly segmentation on MPDD.

Object name	**WinCLIP**	**VAND**	**AnomalyCLIP**	**MPL**	**MPAMA**
Bracket_black	43.0	89.7	85.2	87.3	88.9
Bracket_brown	25.0	70.3	77.7	77.4	81.3
Bracket_white	57.6	93.1	98.8	98.1	98.8
Connector	44.6	74.5	89.8	89.3	88.4
Metal_plate	78.2	74.5	86.9	88.8	86.9
Tubes	44.7	96.9	93.6	88.9	90.4
Mean	48.9	83.2	88.7	88.3	89.2

Table 19: Subset-level performance comparison (AUROC) for anomaly classification on MPDD.

Object name	**WinCLIP**	**VAND**	**AnomalyCLIP**	**MPL**	**MPAMA**
Bracket_black	41.5	66.1	67.3	68.6	71.1
Bracket_brown	48.6	64.0	62.2	61.6	63.0
Bracket_white	40.2	79.6	64.9	78.7	80.7
Connector	79.3	78.8	86.9	82.4	81.5
Metal_plate	93.4	53.8	85.2	88.5	91.8
Tubes	78.7	95.9	95.5	96.5	99.2
Mean	63.6	73.0	77.0	79.4	81.2

Table 20: Subset-level performance comparison (AP) for anomaly classification on MPDD.

Object name	WinCLIP	VAND	AnomalyCLIP	MPA	MPAMA
Bracket_black	56.9	71.7	72.9	75.7	75.7
Bracket_brown	69.5	79.0	80.8	76.5	78.5
Bracket_white	45.1	82.3	68.5	76.4	76.3
Connector	61.3	71.8	76.8	67.0	65.1
Metal_plate	97.6	78.3	94.7	94.9	97.3
Tubes	89.1	98.1	98.1	98.0	99.5
Mean	69.9	80.2	82.0	81.4	82.1

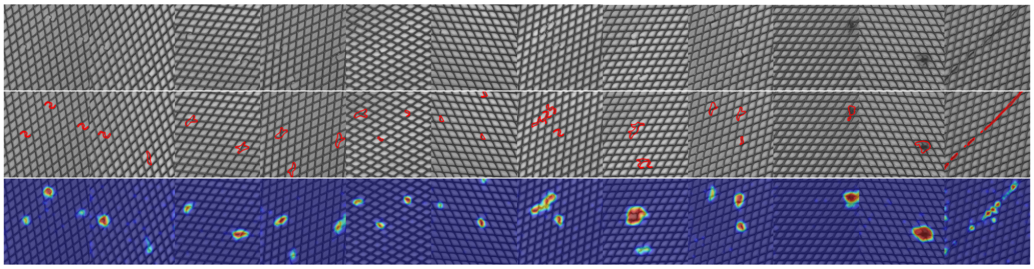

Figure 10: Anomaly segmentation for the 'grid' subset of MVTec AD. The first row shows the input images, the second row highlights anomaly regions with red contours, and the third row displays the segmentation results from MPAMA.

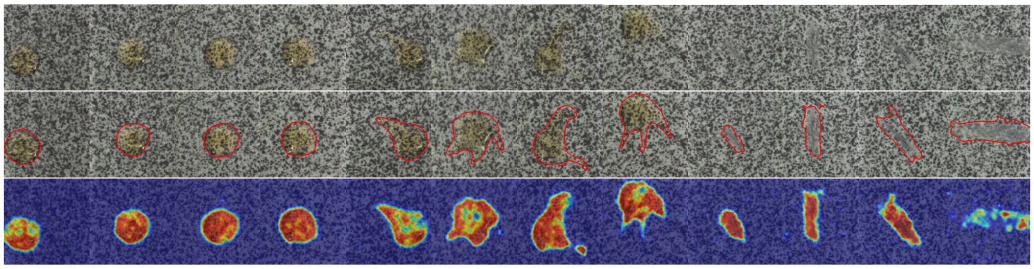

Figure 11: Anomaly segmentation for the 'skin' subset of ISIC. The first row shows the input images, the second row highlights anomaly regions with red contours, and the third row displays the segmentation results from MPAMA.

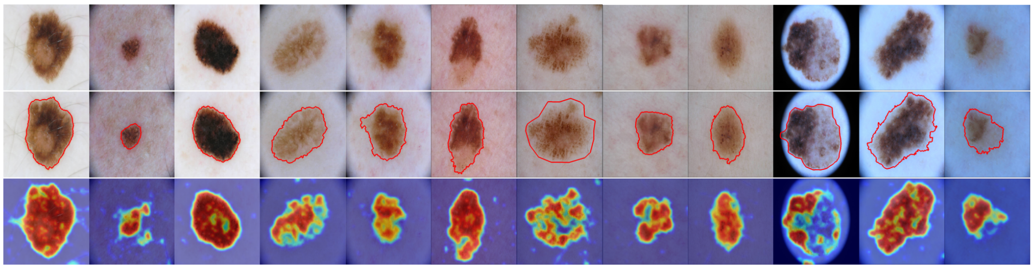

Figure 12: Anomaly segmentation for the 'tile' subset of MVTec AD. The first row shows the input images, the second row highlights anomaly regions with red contours, and the third row displays the segmentation results from MPAMA.

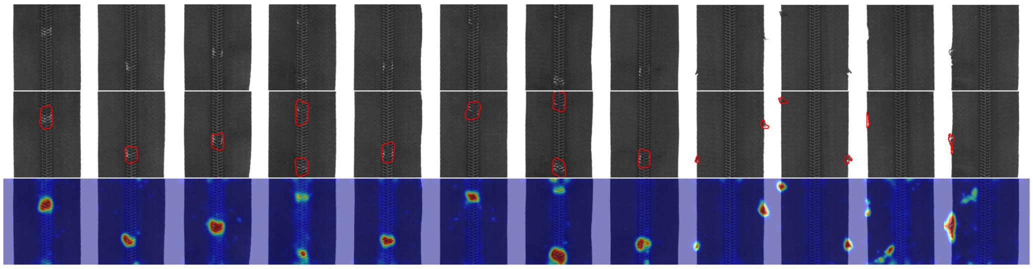

Figure 13: Anomaly segmentation for the 'zipper' subset of MVTec AD. The first row shows the input images, the second row highlights anomaly regions with red contours, and the third row displays the segmentation results from MPAMA.

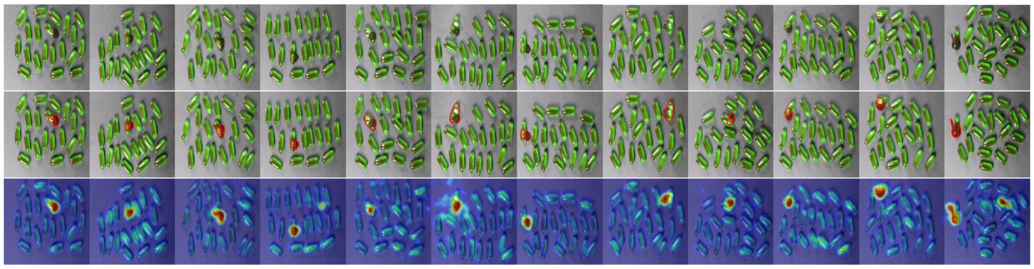

Figure 14: Anomaly segmentation for the ’capsule’ subset of VisA. The first row shows the input images, the second row highlights anomaly regions with red contours, and the third row displays the segmentation results from MPAMA.

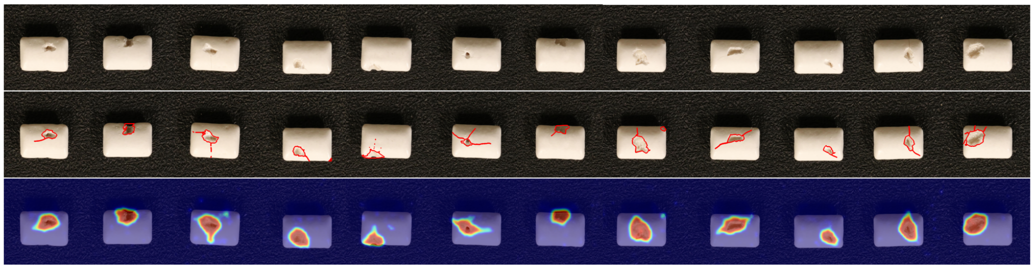

Figure 15: Anomaly segmentation for the ’chewinggum’ subset of VisA. The first row shows the input images, the second row highlights anomaly regions with red contours, and the third row displays the segmentation results from MPAMA.

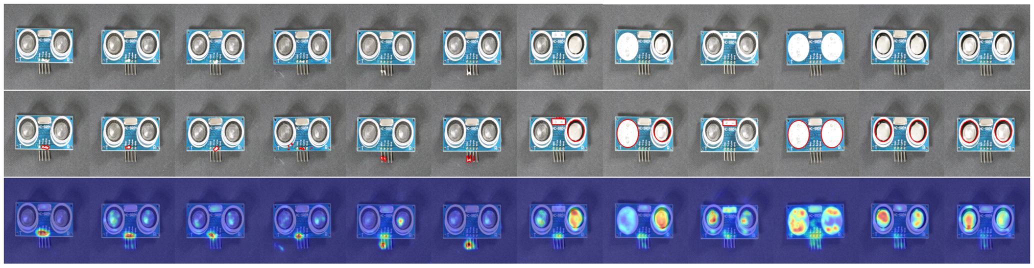

Figure 16: Anomaly segmentation for the ’pcb1’ subset of VisA. The first row shows the input images, the second row highlights anomaly regions with red contours, and the third row displays the segmentation results from MPAMA.

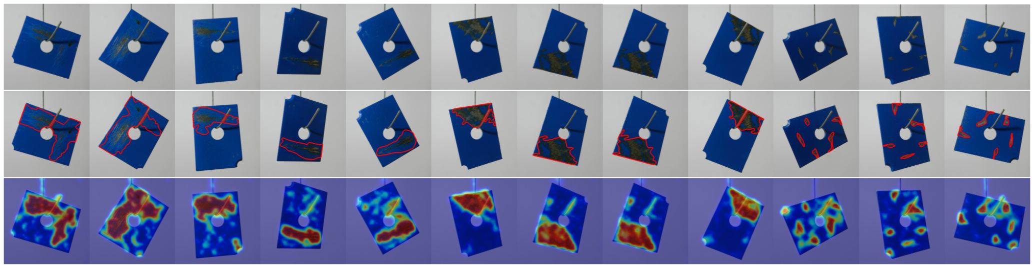

Figure 17: Anomaly segmentation for the ’meta-plate’ subset of VisA. The first row shows the input images, the second row highlights anomaly regions with red contours, and the third row displays the segmentation results from MPAMA.

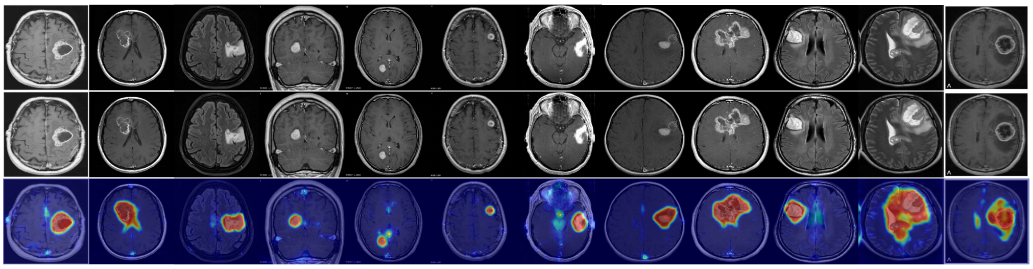

Figure 18: Anomaly segmentation for the ’brain’ subset of HeadCT. The first row shows the input images, the second row highlights anomaly regions with red contours, and the third row displays the segmentation results from MPAMA.